Missing nuclear correlations (i.e. a lack of complexity in nuclear wave functions owing to limitations of nuclear models) as well as neglected contributions from meson-exchange currents (i.e. coupling of the weak force to two nucleons) have been proposed as possible causes of the quenching phenomenon [4]. However, a solution has so far remained elusive. To address the quenching puzzle, we carry out a comprehensive study of Gamow-Teller decays through many-body computations of nuclei based on effective field theories (EFTs) of quantum chromodynamics [7, 19], including an unprecedented amount of correlations in the nuclear wave functions. The EFT approach offers the prospects of accuracy, by encoding the excluded high-energy physics through coefficients adjusted to data, and precision from the systematically improvable EFT expansion. Moreover, EFT enables a consistent description of the coupling of weak interactions to two nucleons, via two-body currents (2BC). In the EFT approach, 2BC enter as subleading corrections to the one-body standard Gamow-Teller operator $\boldsymbol{\sigma}\boldsymbol{\tau}^+$ (with Pauli spin and isospin matrices $\boldsymbol{\sigma}$ and $\boldsymbol{\tau}$, respectively); they are smaller but significant corrections to weak transitions as three-nucleon forces are smaller but significant corrections to the nuclear interaction [7, 19].

In this work we focus on strong Gamow-Teller transitions, where the effects of quenching should dominate over cancellations due to fine details (as occur in the famous case of the $^{14}$C decay used for radiocarbon dating [20, 21]). An excellent example is the super-allowed $\beta$-decay of the doubly magic $^{100}$Sn nucleus (see Fig. 1), exhibiting the strongest Gamow-Teller strength so far measured in all atomic nuclei [5]. A first-principles description of this exotic decay, in such a heavy nucleus, presents a significant computational challenge. However, its equal 'magic' number ($Z = N = 50$) of protons and neutrons arranged into complete shells makes $^{100}$Sn an ideal candidate for large-scale coupled-cluster calculations [22], while the daughter nucleus $^{100}$In can be reached via novel extensions of high-order charge-exchange coupled-cluster methods developed in this work (see Methods and Figs. 5, 12, and 15 in Supplementary Information for details). This method includes correlations via a vast number of particle-hole excitations of a reference state and also employs 2BC in the transition operator.

Figure 1 shows our results for the strength (i.e., the absolute square of the transition matrix element, $M_{\rm GT}$) of the Gamow-Teller transition to the dominant $J^\pi = 1^+$ state in the $^{100}$In daughter nucleus (see Table I and Fig. 12 in Supplementary Information for more details). To investigate systematic trends and sensitivities to the nuclear Hamiltonian, we employed a family of established EFT interactions and corresponding currents [23–25]. For an increased precision, we also developed a new interaction labeled NN-N$^4$LO+3N$_{\rm lnl}$ which is constrained to reproduce the triton half-life (see Methods for details on the Hamiltonians considered). The hollow symbols in Fig. 1 depict the decay with the standard, leading-order coupling of the weak force to a single nucleon in the non-relativistic limit (i.e., via the standard Gamow-Teller operator $\boldsymbol{\sigma}\boldsymbol{\tau}^+$). The differences with respect to the extreme single-particle model (ESPM), which approximates both $^{100}$Sn and its $^{100}$In daughter as a single shell-model configuration, reveals the influence of correlations among the nucleons. The full symbols include 2BC, using consistent couplings as in the employed EFT interactions. Finally, the partially filled symbols in Fig. 1 represent results from other models of Ref. [5], where the standard Gamow-Teller operator was multiplied by a quenching factor $q \sim 0.75$.

Based on our results shown in Fig. 1, we predict the range $5.2(5) \lesssim |M_{\rm GT}|^2 \lesssim 7.0(7)$ for the Gamow-Teller strength. This range overlaps with the evaluation of Batist *et al.* [6], based on systematic experimental trends in the tin isotopes, and the lower end of the measurement by Hinke *et al.* [5]. The quenching factor we obtain from 2BC depends somewhat on the employed Hamiltonian, and is in the range $q_{\rm 2BC} = 0.73 - 0.85$. This range is consistent with the value $q = 0.75(2)$ from Batist *et al.* [6]. In the present work, we used the spread of results obtained with the selected set of EFT interactions and 2BC as an estimate of the systematic uncertainty. A more thorough quantification of the uncertainties associated with the many-body methods and EFT truncations is beyond the scope of this work, and will be addressed in future studies. We note that neglected higher-order correlations in our coupled-cluster approach will further reduce the Gamow-Teller strength (see Supplementary Information for details).

Moreover, we observe that the spread for the $^{100}$Sn Gamow-Teller strength obtained for the family of employed EFT interactions is significantly reduced (by a factor two) when 2BC are included. This is consistent with ideas from EFT that residual cutoff dependence is due to neglected higher-order terms in the Hamiltonian and 2BC. In addition, we find that the relative contributions to the quenching of the Gamow-Teller strength coming from correlations and 2BC vary as a function of the resolution scale of the underlying EFT interactions. Starting from the extreme single-particle model, and adding first correlations and then the effects of 2BC, we find that the quenching from correlations typically increases with increasing resolution scale of the interaction, and that most of the quenching stems from correlations. However, adding first the effects of 2BC and then correlations shows that the quenching from 2BC increases with decreasing resolution scale and that most of the quenching stems from 2BC for all but the "hardest" potentials considered in this work (see Fig. 6 in Supplementary Information for details).

For a comprehensive study, we now turn to $\beta$-decays of light and medium-mass nuclei. Using a selection of

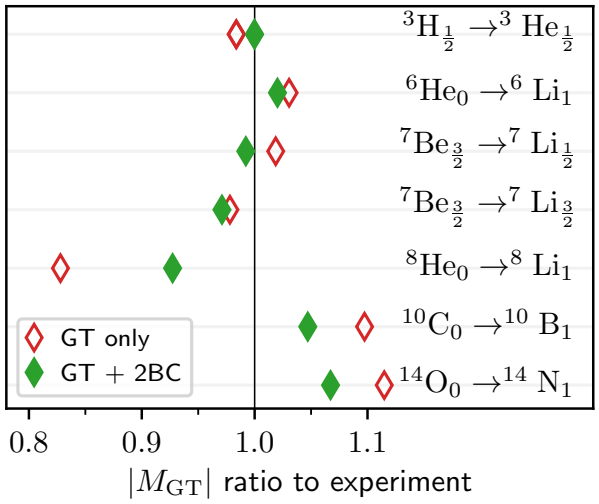


FIG. 2. Theory-to-experiment ratio for the Gamow-Teller matrix elements of six strong transitions in light nuclei for the NN-N$^4$LO+3N$_{\rm lnl}$ interaction developed in this work. The subscripts in the legend denote the total angular momenta of the parent and daughter states. All initial states are ground states. In the case of $^3$H$\rightarrow^3$He, $^6$He$\rightarrow^6$Li and $^7$Be$\rightarrow^7$Li$_{\frac{3}{2}}$, the daughter nucleus is in its ground state, while the $^7$Be$\rightarrow^7$Li$_{\frac{1}{2}}$, $^8$He$\rightarrow^8$Li$_1$ and $^{10}$C$\rightarrow^{10}$B$_1$ are decays to the first excited state of the daughter nucleus, and the $^{14}$O$\rightarrow^{14}$N$_1$ is a decay to the second excited state of $^{14}$N. Hollow symbols correspond to results obtained with the standard Gamow-Teller $\boldsymbol{\sigma\tau}$ operator, and full symbols include 2BC.

the EFT interactions and 2BC adopted for $^{100}$Sn, we achieved an overall good description of $\beta$-decays in light nuclei. Figure 2 shows theory-to-experiment ratios for large Gamow-Teller transitions in light nuclei. Here we highlight the results obtained for the high-precision NN-N$^4$LO+3N$_{\rm lnl}$ interaction and corresponding 2BC developed in this work. As detailed in Methods, the 2BC and three-nucleon forces 3N$_{\rm lnl}$ are parametrized consistently and are constrained to reproduce the empirical value of the triton $\beta$-decay half life. Our calculations were carried out with the no-core shell model [8], a virtually exact treatment of correlations in the nuclear wave functions (see Methods for details). The role of 2BC is relatively small in light nuclei with mass numbers $A \leqslant 7$. Full nuclear wave functions already provide a rather satisfactory description of the transitions with the standard Gamow-Teller operator. Furthermore, the inclusion of 2BC may enhance (e.g., $^8$He$\rightarrow^8$Li), quench (e.g., $^7$Be$_{\frac{3}{2}} \rightarrow^7$Li$_{\frac{1}{2}}$), or have virtually no impact on the computed transition (e.g., $^7$Be$_{\frac{3}{2}} \rightarrow^7$Li$_{\frac{3}{2}}$, see also Fig. 14 in Supplementary Information). The small role of 2BC in $A \leqslant 7$ nuclei is similar to what was found in the Green's function Monte Carlo calculations of Ref. [26]. We find a rather substantial enhancement of the $^8$He Gamow-Teller matrix element due to the 2BC. Let us mention, though, that this transition matrix element is the smallest of those presented in Fig. 2. We note that for the other Hamiltonians employed in this work, the 2BC and 3N were not fit to reproduce the triton half-life, nevertheless the inclusion of 2BC for most of these cases also improves the agreement with data for the light nuclei considered in Fig. 2 (see Fig. 9 in Supplementary Information for results obtained with NNLO$_{\rm sat}$ and NN-N$^3$LO+3N$_{\rm lnl}$). The case of $^{10}$C is special because the computed Gamow-Teller transition is very sensitive to the structure of the $J^\pi = 1^+$ state in the $^{10}$B daughter nucleus. Depending on the employed interaction, this state can mix with a higher-lying $1^+$ state, greatly impacting the precise value of this transition. We finally note that benchmark calculations between the many-body methods used in this work agree to within 5% for the large transition in $^{14}$O. For smaller transitions discrepancies can be larger (see Supplementary Information for details).

Historically, the most extensive evidence for the quenching of Gamow-Teller $\beta$-decay strength comes from medium-mass nuclei [16, 18, 29], and we now show that our calculations with these consistent Hamiltonians and currents largely solves the puzzle here as well. We use the valence-space in-medium similarity renormalization group (VS-IMSRG) method [64] (see Methods for details) and compute Gamow-Teller decays for nuclei in the mass range between oxygen and calcium (referred to as *sd*-shell nuclei) and between calcium and vanadium (lower *pf*-shell nuclei), focusing on strong transitions. Here, we highlight the NN-N$^4$LO+3N$_{\rm lnl}$ interaction and corresponding 2BC.

Figure 3 shows the empirical values of the Gamow-Teller transition matrix elements versus the corresponding unquenched theoretical matrix elements obtained from phenomenological shell model with the standard Gamow-Teller $\boldsymbol{\sigma\tau}$ operator and the first-principles VS-IMSRG calculations. Perfect agreement between theory and experiment is denoted by the diagonal dashed line. The results from the phenomenological shell model clearly exemplify the state of theoretical calculations for decades [15–18, 29], as an example, in the *sd*-shell shell, a quenching factor of $q \sim 0.8$ is needed to bring the theory into agreement with experiment [16]. The VS-IMSRG calculations without 2BC (not shown) exhibit a modest improvement, with a corresponding quenching factor of 0.89(4) for *sd*-shell nuclei and 0.85(3) for *pf*-shell nuclei, pointing to the importance of consistent valence-space wave functions and operators (see Fig.10 in Supplementary Information). As in $^{100}$Sn, the inclusion of 2BC yields an additional quenching of the theoretical matrix elements, and the linear fit of our results lies close to the dashed line, meaning our theoretical predictions agree on average with experimental values across a large number of medium-mass nuclei.

Another approach often used in the investigation of

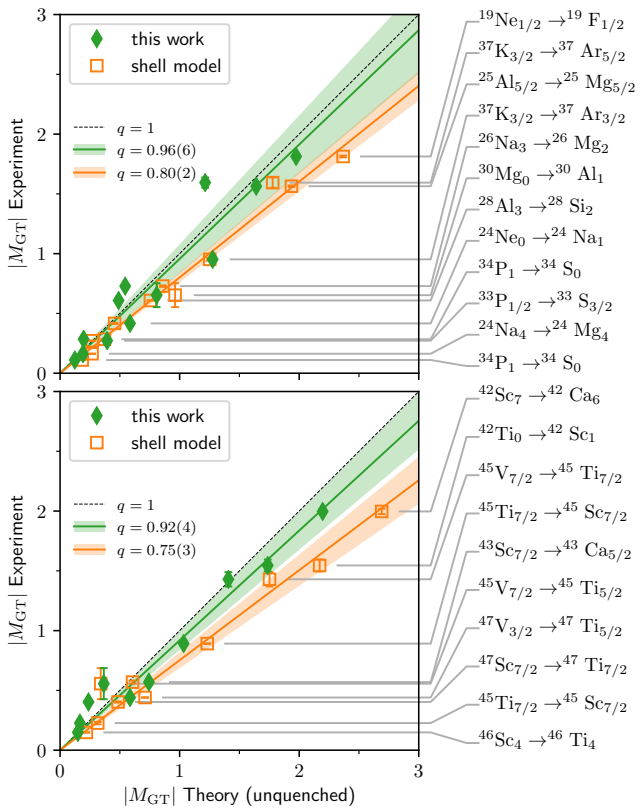


FIG. 3. Comparison of experimental [27] and theoretical Gamow-Teller matrix elements for medium-mass nuclei in the *sd*-shell (top panel) and lower *pf*-shell (bottom panel). The theoretical results were obtained using phenomenological shell-model interactions [18, 28] with an unquenched standard Gamow-Teller $\boldsymbol{\sigma\tau}$ operator (orange squares); and using the VS-IMSRG approach with the NN-N$^4$LO+3N$_{\rm lnl}$ interaction and consistently evolved Gamow-Teller operator plus 2BC (green diamonds). The linear fits show the resulting quenching factor $q$ given in the panels, and shaded bands indicate one standard deviation from the average quenching factor.

Gamow-Teller quenching is the Ikeda sum-rule: the difference between the total integrated $\beta^-$ and $\beta^+$ strengths obtained with the $\boldsymbol{\sigma\tau}^{\mp}$ operator yields the model-independent sum-rule $3(N-Z)$. We have computed the Ikeda sum-rule for $^{14}$O, $^{48}$Ca, and $^{90}$Zr using the coupled-cluster method (see Methods for details). For the family of EFT Hamiltonians used for $^{100}$Sn we obtain a quenching factor arising from 2BC, which is consistent with our results shown in Fig. 3 and the shell-model analyses from Refs. [16–18, 29] (see Fig. 7 in Supplementary Information). We note that the comparison with experimental sum-rule tests using charge-exchange reactions [30, 31] are complicated by the use of a hadronic probe, which only corresponds to the leading weak one-body operator, and by the challenge of extracting all strength to high energies. Here, our developments enable future direct comparisons.

It is the combined proper treatment of strong nuclear correlations with powerful quantum many-body solvers and the consistency between 2BC and three-nucleon forces that largely explains the quenching puzzle. Smaller corrections are still expected to arise from neglected higher order contributions to currents and Hamiltonians in the EFT approach we pursued, and from neglected correlations in the nuclear wave functions. For beyond-standard-model searches of new physics such as neutrinoless double-$\beta$ decay, our work suggests that a complete and consistent calculation without a phenomenological quenching of the axial-vector coupling $g_A$ is called for. This Letter opens the door to ab initio calculations of weak interactions across the nuclear chart and in stars.


[1] Janka, H.-T., Langanke, K., Marek, A., Martínez-Pinedo, G. & Müller, B. Theory of core-collapse supernovae. *Phys. Rep.* **442**, 38 – 74 (2007).

[2] Schatz, H. *et al.* Strong neutrino cooling by cycles of electron capture and $\beta$-decay in neutron star crusts. *Nature* **505**, 62–65 (2013).

[3] Engel, J. & Menéndez, J. Status and future of nuclear matrix elements for neutrinoless double-beta decay: a review. *Rep. Prog. Phys.* **80**, 046301 (2017).

[4] Towner, I. S. Quenching of spin matrix elements in nuclei. *Phys. Rep.* **155**, 263 – 377 (1987).

[5] Hinke, C. B. *et al.* Superallowed Gamow-Teller decay of the doubly magic nucleus $^{100}$Sn. *Nature* **486**, 341–345 (2012).

[6] Batist, L. *et al.* Systematics of Gamow-Teller beta decay Southeast of $^{100}$Sn. *Eur. Phys. J. A* **46**, 45–53 (2010).

[7] Epelbaum, E., Hammer, H.-W. & Meißner, U.-G. Modern theory of nuclear forces. *Rev. Mod. Phys.* **81**, 1773–1825 (2009).

[8] Barrett, B. R., Navrátil, P. & Vary, J. P. Ab initio no core shell model. *Prog. Part. Nucl. Phys.* **69**, 131 – 181 (2013).

[9] Hagen, G. *et al.* Neutron and weak-charge distributions of the $^{48}$Ca nucleus. *Nature Phys.* **12**, 186–190 (2016).

[10] Stroberg, S. R. *et al.* Nucleus-dependent valence-space approach to nuclear structure. *Phys. Rev. Lett.* **118**, 032502 (2017).

[11] Korobkin, O., Rosswog, S., Arcones, A. & Winteler, C. On the astrophysical robustness of the neutron star merger r-process. *Monthly Notices of the Royal Astronomical Society* **426**, 1940–1949 (2012).

[12] Mumpower, M. R., Surman, R., McLaughlin, G. C. & Aprahamian, A. The impact of individual nuclear properties on r-process nucleosynthesis. *Prog. Part. Nucl. Phys.* **86**, 86 – 126 (2016).

[13] Pian, E. *et al.* Spectroscopic identification of r-process nucleosynthesis in a double neutron-star merger. *Nature* **551**, 67–70 (2017).

[14] Barea, J., Kotila, J. & Iachello, F. Limits on neutrino masses from neutrinoless double-$\beta$ decay. *Phys. Rev. Lett.* **109**, 042501 (2012).

[15] Wilkinson, D. H. Renormalization of the axial-vector coupling constant in nuclear $\beta$-decay (ii). *Nucl. Phys. A*

**209**, 470 – 484 (1973).
[16] Brown, B. A. & Wildenthal, B. H. Experimental and theoretical Gamow-Teller beta-decay observables for the sd-shell nuclei. *Atomic Data and Nuclear Data Tables* **33**, 347 – 404 (1985).
[17] Chou, W.-T., Warburton, E. K. & Brown, B. A. Gamow-Teller beta-decay rates for $A \leq 18$ nuclei. *Phys. Rev. C* **47**, 163–177 (1993).
[18] Martínez-Pinedo, G., Poves, A., Caurier, E. & Zuker, A. P. Effective $g_A$ in the $pf$ shell. *Phys. Rev. C* **53**, R2602–R2605 (1996).
[19] Machleidt, R. & Entem, D. R. Chiral effective field theory and nuclear forces. *Phys. Rep.* **503**, 1 – 75 (2011).
[20] Holt, J. W., Kaiser, N. & Weise, W. Chiral three-nucleon interaction and the $^{14}$C-dating $\beta$ decay. *Phys. Rev. C* **79**, 054331 (2009).
[21] Maris, P. *et al.* Origin of the anomalous long lifetime of $^{14}$C. *Phys. Rev. Lett.* **106**, 202502 (2011).
[22] Morris, T. D. *et al.* Structure of the lightest tin isotopes. *Phys. Rev. Lett.* **120**, 152503 (2018).
[23] Hebeler, K., Bogner, S. K., Furnstahl, R. J., Nogga, A. & Schwenk, A. Improved nuclear matter calculations from chiral low-momentum interactions. *Phys. Rev. C* **83**, 031301 (2011).
[24] Ekström, A. *et al.* Accurate nuclear radii and binding energies from a chiral interaction. *Phys. Rev. C* **91**, 051301 (2015).
[25] Leistenschneider, E. *et al.* Dawning of the $N = 32$ shell closure seen through precision mass measurements of neutron-rich titanium isotopes. *Phys. Rev. Lett.* **120**, 062503 (2018).
[26] Pastore, S. *et al.* Quantum Monte Carlo calculations of weak transitions in $A = 6 - 10$ nuclei. *Phys. Rev. C* **97**, 022501 (2018).
[27] Data retrieved using the NNDC On-Line Data Service from the ENSD database, file revised as of Oct 5 2018. Bhat, M. R. Evaluated Nuclear Structure Data File (ENSDF). In Qaim, S. M. (ed.) *Nuclear Data for Science and Technology*, 817 (Springer-Verlag, 1992).
[28] Brown, B. A. & Richter, W. A. New "USD" Hamiltonians for the *sd* shell. *Phys. Rev. C* **74**, 034315 (2006).
[29] Langanke, K., Dean, D. J., Radha, P. B., Alhassid, Y. & Koonin, S. E. Shell-model monte carlo studies of fp-shell nuclei. *Phys. Rev. C* **52**, 718–725 (1995).
[30] Gaarde, C. *et al.* Excitation of giant spin-isospin multipole vibrations. *Nucl. Phys. A* **369**, 258 – 280 (1981).
[31] Wakasa, T. *et al.* Gamow-Teller strength of $^{90}$Nb in the continuum studied via multipole decomposition analysis of the $^{90}$Zr$(p, n)$ reaction at 295 MeV. *Phys. Rev. C* **55**, 2909–2922 (1997).

**Acknowledgments** We thank H. Grawe and T. Faestermann for useful correspondance, J. Engel, E. Epelbaum, D. Gazit, H. Krebs, D. Lubos, S. Pastore, and R. Schiavilla for useful discussions, and K. Hebeler for providing us with matrix elements in Jacobi coordinates for the three-nucleon interaction at next-to-next-to-leading order [23]. This work was prepared in part by Lawrence Livermore National Laboratory (LLNL) under Contract DE-AC52-07NA27344 and was supported by the Office of Nuclear Physics, U.S. Department of Energy, under Grants DE-FG02-96ER40963, DE-FG02-97ER41014, de-sc0008499, de-sc0018223, de-sc0015376, the Field Work Proposals ERKBP57 and ERKBP72 at Oak Ridge National Laboratory (ORNL), the FWP SCW1579, LDRD projects 18-ERD-008 and 18-ERD-058 and the Lawrence Fellowship Program at LLNL, and by the NSERC Grant No. SAPIN-2016-00033, the ERC Grant No. 307986 STRONGINT, and the DFG under Grant SFB 1245. TRIUMF receives federal funding via a contribution agreement with the National Research Council of Canada. Computer time was provided by the Innovative and Novel Computational Impact on Theory and Experiment (INCITE) program. This research used resources of the Oak Ridge Leadership Computing Facility located at ORNL, which is supported by the Office of Science of the Department of Energy under Contract No. DE-AC05-00OR22725. Computations were also performed at the LLNL Livermore Computing under the institutional Computing Grand Challenge Program, at Calcul Quebec, Westgrid and Compute Canada, and at the Jülich Supercomputing Center (JURECA).

**Author contributions** G.H., T.D.M., and T.P. performed the coupled-cluster calculations. G.R.J. computed three-nucleon forces for the coupled-cluster calculations. P.G., S.Q., P.N., and K.A.W. performed calculations for the two-body currents. P.N. developed higher precision chiral three-nucleon interactions used in this work and performed no-core shell model calculations. G.H. and T.D.M. derived and implemented new formalism to incorporate higher-order excitations in coupled-cluster theory. S.R.S. and J.D.H. performed VS-IMSRG calculations. All authors discussed the results and contributed to the manuscript at all stages.

**Author information** Reprints and permissions information is available at www.nature.com/reprints. The authors declare no competing financial interests. Readers are welcome to comment on the online version of the paper. Correspondence and requests for materials should be addressed to G.H. (hageng@ornl.gov)

## METHODS

**Hamiltonians and model space.** In this work we employ the intrinsic Hamiltonian

$$H = \sum_{i<j} \left( \frac{(\mathbf{p}_i - \mathbf{p}_j)^2}{2mA} + V_{\rm NN}^{(i,j)} \right) + \sum_{i<j<k} V_{\rm 3N}^{(i,j,k)}. \quad (1)$$

Here $\mathbf{p}_i$ is the nucleon momentum, $m$ the average nucleon mass, $A$ the mass number of the nucleus of interest, $V_{\rm NN}$ the nucleon-nucleon (NN) interaction, and $V_{\rm 3N}$ the three-nucleon (3N) interaction.

We use a set of interactions from Ref. [23] labeled 1.8/2.0 (EM), 2.0/2.0 (EM), 2.2/2.0 (EM), 2.8/2.0 (EM), and 2.0/2.0 (PWA). These consist of a chiral NN interaction at order N$^3$LO from Ref. [32] evolved to the resolution scales $\lambda_{\rm SRG} = 1.8, 2.0, 2.2, 2.8$ fm$^{-1}$ by means of the similarity renormalization group (SRG) [33] plus a chiral 3N interaction (unevolved) at order N$^2$LO, using a non-local regulator with momentum cutoff $\Lambda_{\rm 3N} = 2.0$ fm$^{-1}$. Note that the 2.0/2.0 (PWA) interaction employs different long-range pion couplings in the NN and 3N sectors. The low-energy couplings entering these interactions were adjusted to reproduce NN scattering data as well as the $^3$H binding energy and $^4$He charge radius. With the exception of 2.8/2.0 (EM), this set of interactions was recently used to describe binding energies and spectra of neutron-rich nuclei up to $^{78}$Ni [34, 35] and of neutron-deficient nuclei around $^{100}$Sn [22]. The results with the 1.8/2.0 (EM) interaction in particular reproduce ground-state energies very well.

In addition, we also employ the NNLO$_{\rm sat}$ interaction, which was constrained to reproduce nuclear binding energies and charge radii of selected *p*- and *sd*-shell nuclei [24]. *Ab initio* calculations based on NNLO$_{\rm sat}$ accurately describe both radii and binding energies of light- and medium-mass nuclei [9], [36, 37].

Finally, we employ two consistently SRG-evolved NN and 3N interactions, namely NN-N$^3$LO+3N$_{\rm lnl}$ [25] and the NN-N$^4$LO+3N$_{\rm lnl}$ introduced in this work. The NN interactions at N$^3$LO and N$^4$LO are from Refs. [32] and [38], respectively. The 3N interactions 3N$_{\rm lnl}$ use a mixture of local [39] and non-local regulators. The local cutoff is 650 MeV, while the nonlocal cutoff of 500 MeV is the same as in the NN interactions. In case of the NN-N$^4$LO+3N$_{\rm lnl}$, the parameters of the two-pion-exchange 3N forces ($c_1$, $c_3$, and $c_4$) are shifted with respect to their values in the NN potential following the recommendation of Ref. [38]. The couplings of the shorter-range 3N forces ($c_D$ and $c_E$) are constrained to the binding energies and radii of the triton and $^4$He in the NN-N$^3$LO+3N$_{\rm lnl}$ model, and to the triton half-life and binding energy in the NN-N$^4$LO+3N$_{\rm lnl}$ model. We note, however, that the NN-N$^3$LO+3N$_{\rm lnl}$ interaction also reprodces the triton half-life as shown in Fig. 9. The NN and 3N interactions are consistently SRG evolved to the lower cutoff $\lambda_{\rm SRG} = 2.0\,{\rm fm}^{-1}$ (or $\lambda_{\rm SRG} = 1.8\,{\rm fm}^{-1}$ in case of some of our light nuclei calculations).

In our no-core shell model calculations of light nuclei we employ the harmonic-oscillator basis varied in the range $N_{\rm max} = 4 - 14$ and with frequency $\hbar\omega = 20$ MeV. In our coupled-cluster and valence-space IMSRG calculations we start from a Hartree-Fock basis built from the harmonic-oscillator basis with model-space parameters in the range $N_{\rm max} = 6 - 14$ and $\hbar\omega = 12 - 16$ MeV, respectively. Finally, the 3N interaction is truncated to three-particle energies with $E_{\rm 3max} \leqslant 16\hbar\omega$.

**Gamow-Teller transition operator.** The rate at which a Gamow-Teller transition will occur is proportional to the square of the reduced transition matrix element

$$M_{\rm GT} = \langle f | O_{\rm GT} | i \rangle \,. \quad (2)$$

Here $i$ and $f$ label the initial and final states of the mother and daughter nuclei, respectively. (Note that throughout this work, we quote the reduced matrix element $\langle f \| O_{\rm GT} \| i \rangle$, using the Edmonds convention [40]). The transition operator $O_{\rm GT}$ is defined in terms of the $J = 1$ transverse electric multipole $E_1^A(\vec{K})$ of the charge-changing axial-vector current $\vec{J}^A(\vec{K})$

$$O_{\rm GT} = g_{\rm A}^{-1} \sqrt{6\pi} E_1^A(\vec{K} = 0) \,. \quad (3)$$

Here, $\vec{K}$ denotes the momentum transferred to the resulting electron and anti-neutrino pair (or positron and neutrino in $\beta^+$-decay). Because the change in energy between mother and daughter states is typically very small (few MeV) compared to other relevant scales, setting $|\vec{K}| = 0$ is a very good approximation that significantly simplifies the calculation of $M_{\rm GT}$.

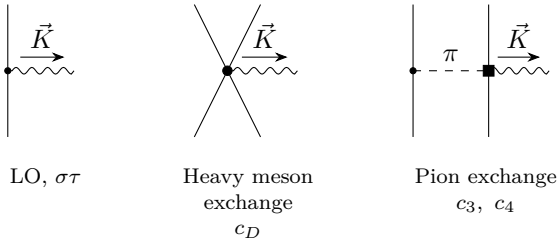


FIG. 4. Diagrammatic representations of terms that contribute to the axial-vector charge-changing current up to N$^2$LO in the limit $\vec{K} \to 0$, up to permutations of the vertices. The solid lines are nucleons, the dashed lines are pions, and the wavy line is the coupling to the electron and anti-neutrino. The leftmost diagram yields the standard (one-body) $\boldsymbol{\sigma\tau}$ transition operator, the other diagrams form the leading 2BC.

The standard (one-body) charge-changing axial-vector current is

$$\vec{J}^A(\vec{K}) = \sum_j \imath g_A \boldsymbol{\sigma}_j \boldsymbol{\tau}_j^{\pm} e^{\imath \vec{K} \cdot \vec{r}_j} \,. \quad (4)$$

Here $\vec{r}_j, \boldsymbol{\sigma}_j, \boldsymbol{\tau}_j^{\pm}$ are the position, Pauli-spin, and charge-raising (lowering) operators for the $j$th particle. In this work we use axial-vector currents derived within the same chiral EFT framework used for the strong interactions, including the leading 2BC [41]. The relevant contributions (at $\vec{K} = 0$) are depicted diagrammatically in Fig. 4. The leftmost diagram corresponds to the leading-order one-body current. In addition, we include two classes of 2BC: a short-range term that shares a parameter ($c_D$) with the one-pion-exchange 3N force, as well as two long-range terms that share parameters ($c_3$ and $c_4$) with the two-pion-exchange NN and 3N forces. Within this framework, the Gamow-Teller operator naturally decomposes into two major terms, the standard one-body current ($O^{1b}_{\sigma\tau} = \boldsymbol{\sigma}\boldsymbol{\tau}^{\pm}$) and a 2BC,

$$O_{\rm GT} = O^{1b}_{\sigma\tau} + O^{2b}_{\rm 2BC}. \tag{5}$$

For each of the chiral EFT Hamiltonians employed in this work, the parameters $c_D$, $c_3$, and $c_4$ are taken consistently in the 3N force and 2BC, and the momentum cutoff for the regularization of the currents, $\Lambda_{\rm 2BC}$, is set to the value used in the non-local regulator of the 3N interaction (see Table VI in Supplementary Information). We found that the choice of a local [42] versus non-local regulator in the 2BC has a negligible effect on the Gamow-Teller transition strength. The majority of our results were obtained using a local regulator. When appropriate, the currents were consistently evolved with the nuclear forces to a lower resolution using the SRG (for NN-N$^3$LO+3N$_{\rm lnl}$ and NN-N$^4$LO+3N$_{\rm lnl}$), keeping only up to two-body contributions. In light nuclei, three- and higher-body SRG-induced terms are very small.

**Quantum many-body methods.** In what follows we describe the many-body methods used in this work: coupled-cluster theory, the no-core shell model, and the IMSRG. The coupled-cluster calculations required new methodological developments, which are described in detail below.

**Coupled-cluster method.** Our coupled-cluster calculations start from a Hamiltonian $H_N$ that is normal-ordered with respect to a single-reference Hartree-Fock state $|\Phi_0\rangle$. We approximate the full 3N interaction by truncating it at the normal-ordered two-body level. This approximation has been shown to work well for light- and medium-mass nuclei [43–45]. The central quantity in the coupled-cluster method is the similarity transformed Hamiltonian $\overline{H}_N = e^{-T} H_N e^{T}$, with $T = T_1 + T_2 + \ldots$ being a linear expansion of particle-hole excitations with respect to the reference state $|\Phi_0\rangle$. The truncation of this expansion at some low-order particle-hole excitation rank is the only approximation that occurs in the coupled-cluster method [46, 47]. The non-Hermitian Hamiltonian $\overline{H}_N$ is correlated and the reference state $|\Phi_0\rangle$ becomes the exact ground-state.

We compute ground and excited states using the CCSDT-1 and EOM-CCSDT-1 approximations [48, 49], respectively. These approximations include iterative singles and doubles and leading-order triples excitations, and capture about 99% of the correlation energy in closed (sub-) shell systems [46]. For the Gamow-Teller transitions and expectation values, we solve for the left ground-state of $\overline{H}_N$

$$\langle\Phi_0|(1+\Lambda), \quad \text{with} \quad \Lambda = \Lambda_1 + \Lambda_2 + \ldots. \tag{6}$$

Here $\Lambda$ is a linear expansion in particle-hole de-excitation operators. We truncate $\Lambda$ at the EOM-CCSDT-1 level consistent with the right CCSDT-1 ground-state solution [49].

The Gamow-Teller transition of a $J^\pi = 0^+$ ground state occupies low-lying $1^+$ states in the daughter nucleus. These states in the daughter nucleus are calculated by employing the charge-exchange equation-of-motion coupled-cluster method [50], and we also include the leading-order three-particle-three-hole excitations as defined by the EOM-CCSDT-1 approximation [49]. The absolute squared Gamow-Teller transition matrix element is then

$$\begin{aligned} |M_{\rm GT}|^2 &= |\langle f|O_{\rm GT}|i\rangle|^2 = \langle f|O_{\rm GT}|i\rangle\langle i|O^\dagger_{\rm GT}|f\rangle \\ &= \langle\Phi_0|L^{1^+}_\mu \overline{O_N}|\Phi_0\rangle\langle\Phi_0|(1+\Lambda)\overline{O^\dagger_N} R^{1^+}_\mu|\Phi_0\rangle. \end{aligned} \tag{7}$$

Here $R^{1^+}_\mu$ is the right and $L^{1^+}_\mu$ the corresponding left excited $1^+$ state in the daughter nucleus, and $\overline{O_N} = e^{-T} O_N e^{T}$ is the similarity transform of the normal-ordered Gamow-Teller operator $O_{\rm GT}$ [see Eq. (5)]. In $O_N$ we approximate the two-body part of the operator $O_{\rm GT}$ at the normal-ordered one-body level, neglecting the residual two-body normal-ordered part [50]. Note that the construction of $\overline{O}_N$ induces higher-body terms, and we truncate $\overline{O}_N$ at the two-body level. This approximation is precise for the case of electromagnetic sum rules in coupled-cluster theory [51].

We evaluate the total integrated Gamow-Teller strengths as a ground-state expectation value

$$S^{\pm} = \langle\Phi_0|(1+\Lambda)\overline{O^\dagger_N}\cdot\overline{O_N}|\Phi_0\rangle. \tag{8}$$

For $O = O^{1b}_{\sigma\tau}$ the Ikeda sum-rule is $S^- - S^+ = 3(N-Z)$. As a check of our code, we have verified that this sum-rule is fulfilled.

The inclusion of triples excitations of the right and left eigenstates $R_\mu$ and $L_\mu$, respectively, is challenging in terms of CPU time and the memory. To limit CPU time, we restrict the employed three-particle–three-hole configurations in the EOM-CCSDT-1 calculations to the vicinity of the Fermi surface. This is done by introducing a single-particle index $\tilde{e}_p = |N_p - N_F|$ that measures the difference between the numbers of oscillator shells $N_p$ of the single-particle state with respect to the Fermi surface $N_F$. We only allow three-particle and three-hole

configurations with $\tilde{E}_{pqr} = \tilde{e}_p + \tilde{e}_q + \tilde{e}_r < \tilde{E}_{3\max}$. This approach yields a rapid convergence in EOM-CCSDT-1 calculations, as seen in Fig. 12 of the Supplementary Information.

The storage of the included three-particle–three-hole amplitudes exceeds currently available resources and had to be avoided. We follow Refs. [52–54] and define an effective Hamiltonian in the $P$ space of singles and doubles excitations, so that no explicit triples amplitudes need be stored. Denoting the $Q$-space as that of all triples excitations below $\tilde{E}_{3\max}$, the right eigenvalue equation can be rewritten as

$$\begin{bmatrix} \overline{H}_{PP} & \overline{H}_{PQ} \\ \overline{H}_{QP} & \overline{H}_{QQ} \end{bmatrix} \begin{bmatrix} R_P \\ R_Q \end{bmatrix} = \omega \begin{bmatrix} R_P \\ R_Q \end{bmatrix}. \tag{9}$$

This yields

$$\overline{H}_{PP} R_P + \overline{H}_{PQ} R_Q = \omega R_P, \tag{10}$$

and

$$\overline{H}_{QP} R_P + \overline{H}_{QQ} R_Q = \omega R_Q. \tag{11}$$

Here we have suppressed the label $\mu$ denoting different excited states. Solving Eq. (11) for the triples component of $R$, and then substituting into Eq. (10), we arrive at

$$\overline{H}_{PP} R_P + \overline{H}_{PQ} (\omega - \overline{H}_{QQ})^{-1} \overline{H}_{QP} R_P = \omega R_P. \tag{12}$$

In the EOM-CCSDT-1 approximation $\overline{H}_{QQ} = \langle T|F|T\rangle$, where $F$ is the Fock matrix. In the Hartree-Fock basis $\overline{H}_{QQ}$ is diagonal, and its inversion is trivial. We solve this energy-dependent, effective Hamiltonian self-consistently to arrive at exact eigenstates of the EOM-CCSDT-1 Hamiltonian. This allows for only one state to be constructed at a time. For the computation of higher spin excited states in the daughter nucleus $^{100}$In, we combine the iterative EOM-CCSDT-1 approach, with a perturbative approach that accounts for all excluded three-particle-three-excitations outside the energy cut $\tilde{E}_{3\max}$. This approach is analogous to the active space coupled cluster methods of [55, 56]. By denoting the $Q'$-space as that of all three-particle-three-hole excitations above $\tilde{E}_{3\max}$, we arrive at the following perturbative non-iterative energy correction,

$$\Delta\omega_\mu = \langle \Phi_0 | L_\mu \overline{H}_{PQ'} (\omega_\mu - \overline{H}_{Q'Q'})^{-1} \overline{H}_{Q'P} R_\mu | \Phi_0 \rangle \,. \tag{13}$$

Here $R_\mu$ and $L_\mu$ are the right and corresponding left EOM-CCSDT-1 eigenstates obtained from diagonalization of the energy-dependent similarity transformed Hamiltonian given in Eq. (12). We label this approach EOM-CCSDt-1, and it drastically improves convergence to the full-space EOM-CCSDT-1 energies (see Fig. 15 in Supplementary Information for details).

**No-core shell-model.** The no-core shell model (NCSM) [8], [57] treats nuclei as systems of $A$ nonrelativistic point-like nucleons interacting through realistic inter-nucleon interactions. All nucleons are active degrees of freedom. The many-body wave function is cast into an expansion over a complete set of antisymmetric $A$-nucleon harmonic-oscillator basis states containing up to $N_{\max}$ harmonic-oscillator excitations above the lowest Pauli-principle-allowed configuration:

$$\left| \Psi_A^{J^\pi T} \right\rangle = \sum_{N=0}^{N_{\max}} \sum_i c_{Ni}^{J^\pi T} \, |ANiJ^\pi T\rangle \ . \tag{14}$$

Here, $N$ denotes the total number of harmonic-oscillator excitations of all nucleons above the minimum configuration, $J^\pi T$ are the total angular momentum, parity, and isospin, and $i$ denotes additional quantum numbers. The sum over $N$ is restricted by parity to either an even or odd sequence. The basis is further characterized by the frequency $\omega$ of the harmonic oscillator. Square-integrable energy eigenstates are obtained by diagonalizing the intrinsic Hamiltonian typically by applying the Lanczos algorithm. In the present work, we used the importance-truncation NCSM [58] to reduce the basis size in the highest $N_{\max}$ spaces of the $A = 10$ and $A = 14$ nucleus calculations.

**Valence-space in-medium similarity renormalization group.** The in-medium similarity renormalization group (IMSRG) [59–61] transforms the many-body Hamiltonian $H$ to a diagonal or block-diagonal form via a unitary transformation $U$, i.e., it generates $\tilde{H} = UHU^\dagger$. To achieve this, one expresses the transformation as the exponential of an anti-Hermitian generator, $U = e^\Omega$. Here $\Omega$ encodes information on the off-diagonal physics to be decoupled [62]. Beginning from some single-reference ground-state configuration $|\Phi_0\rangle$ (e.g., the Hartree-Fock state based on initial interactions), we map the reference to the fully correlated ground state $|\Psi_0\rangle$ via a continuous sequence of such unitary transformations $U(s)$. With no approximations, this gives the exact ground-state energy, but in the IMSRG(2) approximation used here, all operators are truncated at the two-body level.

In the valence-space formulation, VS-IMSRG [63, 64], the unitary transformation is constructed (based on a redefinition of $\Omega$) to in addition decouple a valence-space Hamiltonian $H_{\rm vs}$ from the remainder of the Hilbert space. We use an ensemble reference [64] state for normal ordering to capture the main effects of three-body operators within the valence space. The eigenstates are obtained by a subsequent diagonalization of $H_{\rm vs}$ within the valence space. Furthermore, any general operator $\mathcal{O}$ can then be transformed by $\tilde{\mathcal{O}} = e^\Omega \mathcal{O} e^{-\Omega}$, to produce an effective valence-space operator consistent with the valence-space Hamiltonian [65]. The expectation value of $\mathcal{O}$ between initial and final states is obtained as usual by combining

the matrix elements of $\mathcal{O}$ with the one- and two-body shell-model transition densities. Note that there is some ambiguity about which reference we should take when normal ordering: the parent or the daughter. If we were able to perform the unitary transformation without approximation, either choice should give exactly the same answer, so long as we use the same transformation on the wave functions and the operators. However, because we truncate at the two-body level, the transformation is not unitary and the error made is reference-dependent. Comparing results obtained by normal ordering with respect to the parent or the daughter nucleus then provides a (lower bound) estimate of the error due to the truncation. In this work, we find that the different choices give transition matrix elements that differ on the order of $\sim 5\%$. The results presented are those obtained with the parent as the reference. (As an example, if we use $^{14}$N as the reference, the numbers in the third line of Table III become 1.77, 1.81, 1.88, and 1.87).


[32] Entem, D. R. & Machleidt, R. Accurate charge-dependent nucleon-nucleon potential at fourth order of chiral perturbation theory. *Phys. Rev. C* **68**, 041001 (2003).

[33] Bogner, S. K., Furnstahl, R. J. & Perry, R. J. Similarity renormalization group for nucleon-nucleon interactions. *Phys. Rev. C* **75**, 061001 (2007).

[34] Hagen, G., Jansen, G. R. & Papenbrock, T. Structure of $^{78}$Ni from first-principles computations. *Phys. Rev. Lett.* **117**, 172501 (2016).

[35] Simonis, J., Stroberg, S. R., Hebeler, K., Holt, J. D. & Schwenk, A. Saturation with chiral interactions and consequences for finite nuclei. *Phys. Rev. C* **96**, 014303 (2017).

[36] Lapoux, V. *et al.* Radii and binding energies in oxygen isotopes: A challenge for nuclear forces. *Phys. Rev. Lett.* **117**, 052501 (2016).

[37] Duguet, T., Somà, V., Lecluse, S., Barbieri, C. & Navrátil, P. Ab initio calculation of the potential bubble nucleus $^{34}$Si. *Phys. Rev. C* **95**, 034319 (2017).

[38] Entem, D. R., Machleidt, R. & Nosyk, Y. High-quality two-nucleon potentials up to fifth order of the chiral expansion. *Phys. Rev. C* **96**, 024004 (2017).

[39] Navrátil, P. Local three-nucleon interaction from chiral effective field theory. *Few-Body Systems* **41**, 117–140 (2007).

[40] Edmonds, A. R. *Angular Momentum in Quantum Mechanics* (Princeton University Press, 1957). (Princeton University Press, 1957).

[41] Park, T.-S. *et al.* Parameter-free effective field theory calculation for the solar proton-fusion and hep processes. *Phys. Rev. C* **67**, 055206 (2003).

[42] Gazit, D., Quaglioni, S. & Navrátil, P. Three-nucleon low-energy constants from the consistency of interactions and currents in chiral effective field theory. *Phys. Rev. Lett.* **103**, 102502 (2009).

[43] Hagen, G. *et al.* Coupled-cluster theory for three-body Hamiltonians. *Phys. Rev. C* **76**, 034302 (2007).

[44] Roth, R. *et al.* Medium-mass nuclei with normal-ordered chiral $NN$+3$N$ interactions. *Phys. Rev. Lett.* **109**, 052501 (2012).

[45] Hergert, H. *et al.* In-medium similarity renormalization group with chiral two- plus three-nucleon interactions. *Phys. Rev. C* **87**, 034307 (2013).

[46] Bartlett, R. J. & Musiał, M. Coupled-cluster theory in quantum chemistry. *Rev. Mod. Phys.* **79**, 291–352 (2007).

[47] Hagen, G., Papenbrock, T., Hjorth-Jensen, M. & Dean, D. J. Coupled-cluster computations of atomic nuclei. *Rep. Prog. Phys.* **77**, 096302 (2014).

[48] Lee, Y. S., Kucharski, S. A. & Bartlett, R. J. A coupled cluster approach with triple excitations. *J. Chem. Phys.* **81**, 5906–5912 (1984).

[49] Watts, J. D. & Bartlett, R. J. Economical triple excitation equation-of-motion coupled-cluster methods for excitation energies. *Chem. Phys. Lett.* **233**, 81 – 87 (1995).

[50] Ekström, A. *et al.* Effects of Three-Nucleon Forces and Two-Body Currents on Gamow-Teller Strengths. *Phys. Rev. Lett.* **113**, 262504 (2014).

[51] Miorelli, M., Bacca, S., Hagen, G. & Papenbrock, T. Computing the dipole polarizability of $^{48}$Ca with increased precision. *Phys. Rev. C* **98**, 014324 (2018).

[52] Bloch, C. & Horowitz, J. Sur la détermination des premiers états d'un système de fermions dans le cas dégénéré. *Nucl. Phys.* **8**, 91 – 105 (1958).

[53] Haxton, W. C. & Song, C.-L. Morphing the shell model into an effective theory. *Phys. Rev. Lett.* **84**, 5484–5487 (2000).

[54] Smith, C. E., King, R. A. & Crawford, T. D. Coupled cluster methods including triple excitations for excited states of radicals. *J. Chem. Phys.* **122**, 054110 (2005).

[55] Shen, J. & Piecuch, P. Biorthogonal moment expansions in coupled-cluster theory: Review of key concepts and merging the renormalized and active-space coupled-cluster methods. *Chemical Physics* **401**, 180 – 202 (2012).

[56] Shen, J. & Piecuch, P. Combining active-space coupled-cluster methods with moment energy corrections via the cc(p;q) methodology, with benchmark calculations for biradical transition states. *J. Chem. Phys.* **136**, 144104 (2012).

[57] Navrátil, P., Vary, J. P. & Barrett, B. R. Large-basis ab initio no-core shell model and its application to $^{12}$**C**. *Phys. Rev. C* **62**, 054311 (2000).

[58] Roth, R. & Navrátil, P. *Ab Initio* study of $^{40}$Ca with an importance-truncated no-core shell model. *Phys. Rev. Lett.* **99**, 092501 (2007).

[59] Tsukiyama, K., Bogner, S. K. & Schwenk, A. In-medium similarity renormalization group for nuclei. *Phys. Rev. Lett.* **106**, 222502 (2011).

[60] Tsukiyama, K., Bogner, S. K. & Schwenk, A. In-medium similarity renormalization group for open-shell nuclei. *Phys. Rev. C* **85**, 061304 (2012).

[61] Hergert, H., Bogner, S. K., Morris, T. D., Schwenk, A. & Tsukiyama, K. The in-medium similarity renormalization group: A novel ab initio method for nuclei. *Phys. Rep.* **621**, 165 – 222 (2016).

[62] Morris, T. D., Parzuchowski, N. M. & Bogner, S. K. Magnus expansion and in-medium similarity renormalization group. *Phys. Rev. C* **92**, 034331 (2015).

[63] Bogner, S. K. *et al.* Nonperturbative shell-model interactions from the in-medium similarity renormalization group. *Phys. Rev. Lett.* **113**, 142501 (2014).

[64] Stroberg, S. R. *et al.* Nucleus-dependent valence-space approach to nuclear structure. *Phys. Rev. Lett.* **118**, 032502 (2017).

[65] Parzuchowski, N. M., Stroberg, S. R., Navrátil, P., Hergert, H. & Bogner, S. K. Ab initio. *Phys. Rev. C* **96**, 034324 (2017).

[66] Faestermann, T., Górska, M. & Grawe, H. The structure of $^{100}$Sn and neighbouring nuclei. *Prog. Part. Nucl. Phys.* **69**, 85 – 130 (2013).

[67] Brown, B. A. & Wildenthal, B. H. Status of the Nuclear Shell Model. *Ann. Rev. Nucl. Part. Sci.* **38**, 29–66 (1988).

[68] Ikeda, K., Fujii, S. & Fujita, J. The $(p, n)$ reactions and beta decays. *Phys. Lett.* **3**, 271 – 272 (1963).

[69] Wildenthal, B. H., Curtin, M. S. & Brown, B. A. Predicted features of the beta decay of neutron-rich sd-shell nuclei. *Phys. Rev. C* **28**, 1343–1366 (1983).

[70] Yako, K. *et al.* Gamow-Teller strength distributions in $^{48}$Sc by the $^{48}$Ca$(p, n)$ and $^{48}$Ti$(n, p)$ reactions and two-neutrino double-$\beta$ decay nuclear matrix elements. *Phys. Rev. Lett.* **103**, 012503 (2009).

[71] Menéndez, J., Gazit, D. & Schwenk, A. Chiral two-body currents in nuclei: Gamow-Teller transitions and neutrinoless double-beta decay. *Phys. Rev. Lett.* **107**, 062501 (2011).

[72] Krebs, H., Epelbaum, E. & Meißner, U.-G. Nuclear axial current operators to fourth order in chiral effective field theory. *Ann. Phys.* **378**, 317 – 395 (2017).

# Supplementary Information

### Spectrum of $^{100}$In

Let us present details regarding the quality of our calculation of $^{100}$In, the daughter nucleus of the Gamow-Teller decay of $^{100}$Sn. Unfortunately, only little is known regarding the structure of this nucleus [5]. Figure 5 shows the spectrum of the daughter nucleus $^{100}$In for the 1.8/2.0 (EM) interaction, computed with the EOM-CCSD, EOM-CCSD(T), and EOM-CCSDT-1 methods. While triples (T) correlations only change the excitation energies of quasi-degenerate states, they add about 1 MeV of binding energy to $^{100}$In. Due to the large level density in this odd-odd nucleus, it is difficult to predict the (unknown) ground-state spin. The $\beta$-decay of $^{100}$Sn populates $1^+$ states in the daughter. The excitation energy $E_{1^+} \approx 2.9$ MeV is consistent with data [5]. Overall, the spectrum agrees also with large-scale shell model calculations [66].

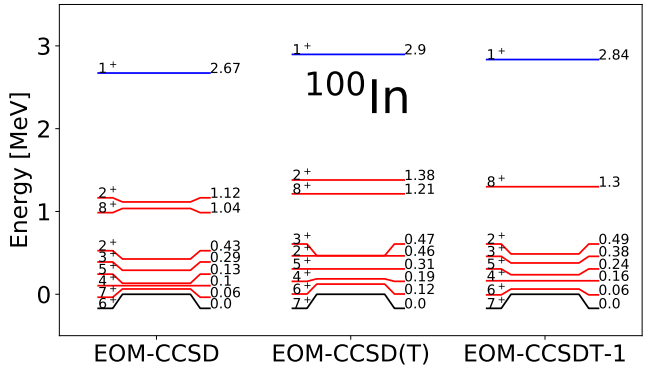


FIG. 5. (Color online) Spectrum of $^{100}$In obtained with the 1.8/2.0 (EM) interaction computed using the EOM-CCSD, EOM-CCSD(T) and EOM-CCSDT-1 methods. The spins/parities and excitation energies (in MeV) of low-lying states and of the $1^+$ state (blue level) populated in the $\beta$ decay of $^{100}$Sn are shown.

### Role of correlations and 2BC in the Gamow-Teller decay of $^{100}$Sn

To throw light onto the quenching puzzle of Gamow-Teller decays, we analyse the contributions of 2BC and strong many-body correlations. Figure 6 analyzes the role of strong correlations and 2BC for the family of EFT interactions employed in this work. This analysis can be done in two ways. First, we can compare the single-particle transition matrix element (ESPM) from the $\nu g_{9/2}$ to the $\pi g_{7/2}$ orbital using the standard Gamow-Teller operator to that with 2BC included, and then finally with the matrix element where correlations are included. This is shown as the lower paths in Fig. 6. Second, we can compare the single-particle transition matrix element from the $\nu g_{9/2}$ to the $\pi g_{7/2}$ orbital using the standard Gamow-Teller operator to the fully correlated transition matrix element using the standard Gamow-Teller operator only ($|M_{\rm GT}(\boldsymbol{\sigma\tau})|^2$), and then to the fully correlated transition matrix element with 2BC included ($|M_{\rm GT}|^2$) as shown in the upper paths. Depending whether one goes along the upper or lower path the role of correlations versus the role of 2BC on the quenching is different. Of course, only the sum of the effects from correlations and 2BC are observable. This analysis shows that the interplay of correlations and 2BC is subtler than often portrayed (when almost always the upper path is considered) [42, 50, 67],[26]. We also note that the contribution from correlations (2BC) to the quenching typically increases (decreases) with increasing resolution scale (i.e. increasing ultraviolet cutoff) of the employed interaction. This is not unexpected, as "hard" interactions introduce more correlations into wave functions and thereby reduce the large transition matrix element one would expect from a transition between two shell-model configurations.

### Summary of results for $^{100}$Sn

Let us summarize our extensive results for the key heavy nucleus $^{100}$Sn. Table I shows the results for the $\beta^+$ decay of $^{100}$Sn to $^{100}$In for the various Hamiltonians employed in this work. The listed observables are the Gamow-Teller strenghts with 2BC ($|M_{\rm GT}|^2$), the log $ft$ values, the Gamow-Teller strengths with the standard Gamow-Teller operator only ($|M_{\rm GT}(\boldsymbol{\sigma\tau})|^2$), the energy difference between the ground state of $^{100}$Sn and the first excited $1^+$ state in the daughter nucleus $^{100}$In, and the binding energy per nucleon ($BE/A$) for the family of EFT interactions employed in this work. For the cases where the binding energy is not converged, we note that the Gamow-Teller operator acts only in spin-isospin space, and is therefore rather insensitive to the tail of the wave functions (which carry information about the binding energy). Benchmark calculations between EOM-CCSDT-1 and NCSM for the Gamow-Teller transition in $^{14}$O show agreement with 3% for three different interactions (see Table III below). Therefore a conservative uncertainty estimate for the Gamow-Teller transition in $^{100}$Sn is about 10%.

TABLE I. Gamow Teller (GT) matrix elements from the extreme single-particle model (ESPM) $|m_{\rm GT}(\boldsymbol{\sigma\tau})|^2$ and EOM-CCSDT-1 $|M_{\rm GT}(\boldsymbol{\sigma\tau})|^2$, sum of GT and 2BC from ESPM $|m_{\rm GT}|^2$ and EOM-CCSDT-1 $|M_{\rm GT}|^2$, the log $ft$ values, the quenching factor $q$ from 2BC from EOM-CCSDT-1 and ESPM, the energy difference between the ground-state of $^{100}$Sn and the $1^+$ state in $^{100}$In, and the binding energy per particle ($BE/A$) in $^{100}$Sn for the interactions used in this work, and compared to experiment. The $BE/A$ obtained with the interactions X/Y (EM) and 2.0/2.0 (PWA) were taken from Ref. [22], the $BE/A$ for the remaining interactions were obtained by employing the same model-space as used for the calculations of $|M_{\rm GT}|^2$, i.e., $N_{\rm max} = 10$ and $E_{3\rm max} = 16$. The energy difference $\Delta E$ were calculated using the model-space $N_{\rm max} = 10$ and $E_{3\rm max} = 16$ for the ground-state (CCSDT-1) and $\tilde{E}_{3\rm max} = 11$ for the $1^+$ excited state (EOM-CCSDT-1) in $^{100}$In. All calculations used the harmonic oscillator frequency $\hbar\omega = 12$MeV.

| Interaction | $\lvert m_{\rm GT}(\boldsymbol{\sigma\tau})\rvert^2$ | $\lvert M_{\rm GT}(\boldsymbol{\sigma\tau})\rvert^2$ | $\lvert m_{\rm GT}\rvert^2$ | $\lvert M_{\rm GT}\rvert^2$ | log $ft$ | $q$ | $q$ (ESPM) | $\Delta E$ [MeV] | $BE/A$ [MeV] |
|---|---|---|---|---|---|---|---|---|---|
| NNLO$_{\rm sat}$ | 17.7 | 8.9 | 12.5 | 6.5 | 2.77 | 0.85 | 0.84 | 7.4 | not converged |
| NN-N$^3$LO+3N$_{\rm lnl}$ | 16.9 | 10.0 | 10.6 | 6.9 | 2.74 | 0.83 | 0.79 | 6.1 | 7.6 |
| NN-N$^4$LO+3N$_{\rm lnl}$ | 17.2 | 10.1 | 8.2 | 5.4 | 2.85 | 0.73 | 0.69 | 5.8 | 7.1 |
| 1.8/2.0 (EM) | 17.7 | 11.3 | 9.8 | 7.0 | 2.73 | 0.79 | 0.74 | 5.1 | 8.4 |
| 2.0/2.0 (EM) | 17.7 | 10.7 | 10.2 | 6.9 | 2.74 | 0.80 | 0.76 | 6.0 | 7.7 |
| 2.0/2.0 (PWA) | 17.7 | 9.9 | 11.5 | 5.9 | 2.81 | 0.77 | 0.81 | 6.8 | 6.4 |
| 2.2/2.0 (EM) | 17.7 | 10.1 | 10.6 | 6.6 | 2.76 | 0.81 | 0.77 | 6.7 | 7.2 |
| 2.8/2.0 (EM) | 17.7 | 7.4 | 11.8 | 5.2 | 2.86 | 0.84 | 0.82 | 8.3 | not converged |
| Batist *et al.* [6] | | | | $5.2 \pm 0.6$ | | | | 5.11 | 8.25 |
| Hinke *et al.* [5] | | | | $9.1^{+2.6}_{-3.0}$ | $2.62^{+0.13}_{-0.11}$ | | | | |

**Results for Ikeda sum-rule**

The Ikeda sum-rule [68] (the difference between the total integrated $\beta^-$ and $\beta^+$ strengths for Gamow-Teller transitions mediated by $\boldsymbol{\sigma\tau}^{\pm}$) gives the model-independent result $3(N-Z)$. Figure 7 shows our coupled-cluster results for the quenching factor $Q \equiv q^2_{\rm 2BC} = (S^- - S^+)/[3(N-Z)]$ for $^{14}$O, $^{48}$Ca, and $^{90}$Zr obtained for the family of EFT Hamiltonians and corresponding 2BC considered in this work (see Methods for details). The total integrated Gamow-Teller strengths $S^{\pm}$ are calculated as a ground-state expectation value by inserting a complete set of intermediate $1^+$ states in the daughter nucleus using the coupled-cluster method (see Methods for details). We note that the Ikeda sum-rule is trivially fulfilled if one employs the standard Gamow-Teller operator $\boldsymbol{\sigma\tau}^{\pm}$. Thus, the quenching factor we obtain for the Ikeda sum-rule is entirely due to 2BC.

In summary, we obtain the quenching factors $q_{\rm 2BC} = 0.90 - 0.94$ for $^{14}$O, $q_{\rm 2BC} = 0.80 - 0.86$ for $^{48}$Ca, and $q_{\rm 2BC} = 0.72 - 0.80$ for $^{90}$Zr, respectively. Our predictions for the quenching factors are consistent with the shell-model analyses of quenched $\beta$-decays in the $p$-shell [17], $sd$-shell [69], and the $pf$-shell [18]. For $^{48}$Ca our results for $S^-$ are in the range $18.5 - 22.6$ and is slightly larger than the measurement $S^- = 15.0 \pm 2.2$ [70]. The measured strength in $^{90}$Zr is $S^- = 28.0 \pm 1.6$ [31] and consistent with our calculated range of $21.5 - 29.6$.

**Role of 2BC and induced many-body terms in light nuclei**

Let us study light nuclei in more detail, because these have been described in several publications [42, 50], [26]. Figure 8 shows the convergence of $^3$H$\rightarrow^3$He and $^6$He$\rightarrow^6$Li Gamow-Teller matrix elements with the NN-N$^4$LO+3N$_{\rm lnl}$ interaction and highligts the size of the SRG induced two-body terms as well as the role of the 2BC. Omitting the SRG-induced two-body contribution of the $\sigma\tau$ operator results in a matrix element dependence on the SRG evolution parameter $\lambda$. This depencence is then removed by the induced two-body terms (i.e., the three- and higher-body induced terms are negligible) from the consistent SRG evolution that at the same time reduce the absolute values of the matrix elements. The (SRG-evolved) 2BC then enhance or quench the Gamow-Teller matrix elements in case of $^3$H$\rightarrow^3$He and $^6$He$\rightarrow^6$Li$_{\frac{1}{2}}$, respectively.

Figure 9 shows theory-to-experiment ratios for strong Gamow-Teller transitions in light nuclei for the NNLO$_{\rm sat}$ and NN-N$^3$LO+3N$_{\rm lnl}$ interactions and corresponding 2BC. For these interactions, the 3N forces and 2BC were not constrained to reproduce the triton half-life.

**Role of 2BC in $sd$- and $pf$-shell nuclei**

Medium-mass nuclei have been key to indficate the quenching puzzle [18, 28, 29]. This makes it important

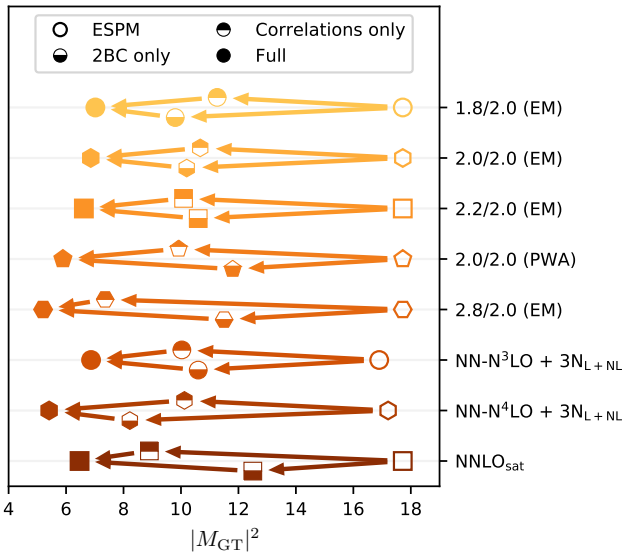


FIG. 6. (Color online) Comparison of the role of correlations versus 2BC for the family of EFT interactions employed in this work. Here the hollow symbols show the single-particle transition matrix element (ESPM) from the $\nu g_{9/2}$ to the $\pi g_{7/2}$ orbitals. The partially filled symbols show the the fully correlated transition matrix element with the standard Gamow-Teller operator only (upper-half filled), and the single-particle transition matrix element from the $\nu g_{9/2}$ to the $\pi g_{7/2}$ orbitals including 2BC (lower-half filled). The filled symbols show the final correlated Gamow-Teller transition matrix element with 2BC included.

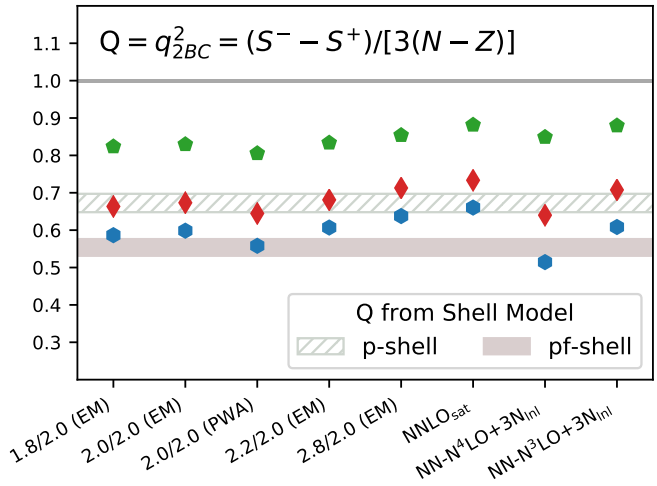


FIG. 7. Predicted quenching, $Q \equiv q^2_{\rm 2BC} = (S^- - S^+)/[3(N-Z)]$, of the Ikeda sum-rule in $^{14}$O (green filled pentagons), $^{48}$Ca (red filled diamonds), and $^{90}$Zr (blue filled hexagons) due to 2BC. The quenching factor is calculated for the family of EFT interactions with corresponding 2BC considered in this work (see Methods for details). The horizontal hatched and shaded areas are quenching factors obtained from the shell-model analyses of $\beta$-decays in the $p$-shell [17] and the $pf$-shell [18], respectively.

to present more details for these nuclei. Figure 10 shows the empirical values of the Gamow-Teller transition matrix elements versus the corresponding theoretical matrix elements obtained with the standard Gamow-Teller $\boldsymbol{\sigma\tau}$ operator (wide diamonds), with the consistently-evolved $\boldsymbol{\sigma\tau}$ operator (narrow diamonds), and the full calculation with the inclusion of 2BC (filled diamonds) for the NN-N$^4$LO+3N$_{\rm lnl}$ interaction. Perfect agreement between theory and experiment is denoted by the diagonal dashed line. We see that both the consistent evolution of the operator (which accounts for correlations beyond the valence space) and the inclusion of 2BC contribute significantly to the quenching effect, consistent with the observations in Figs. 1 and 6.

In order to assess how dependent the quenching effect observed in Fig. 3 is on the choice of input interaction, we repeat the calculation with the NNLO$_{\rm sat}$ interaction. The results, shown in Fig. 11, are consistent with the findings in Fig. 3.

### Benchmarks between methods

In this work we used three complentary methods – the NCSM, the coupled-cluster method, and the VS-IMSRG – to compute nuclei in different regions of the nuclear chart. For binding energies alone, these methods have been benchmarked several times, see, e.g., Refs. [22] and [61]. Here, we also benchmark these methods for Gamow-Teller decays. We focus on the Gamow-Teller decays of the light nuclei $^8$He, $^{10}$C, and $^{14}$O that exhibit considerable impact from 2BC. The coupled-cluster method is limited to nuclei with closed subshells. In light nuclei, this limits us to $^8$He and $^{14}$O, and in medium-mass nuclei we focus on the Gamow-Teller decays of $^{34}$Si and $^{68}$Ni. Our coupled-cluster calculations use the CCSDT-1 approximation. The presented NCSM results are converged to within 3% with respect to the model-space size.

Table II shows the the transition in $^8$He to the first $1^+_1$ state in $^8$Li using the NN-N$^4$LO +3N$_{\rm lnl}$ interaction. Here $M_{\rm GT}(\boldsymbol{\sigma\tau})$ denotes the matrix element of the $\boldsymbol{\sigma\tau}$ operator, while $M_{\rm GT}$ includes 2BC. The NCSM and coupled-cluster triples results are within a few percent of each other, while VS-IMSRG is within about 30% of the NCSM.

Table III shows the transition in $^{14}$O to the second $1^+_2$ state in $^{14}$Ni using the NNLO$_{\rm sat}$ and the NN-N$^4$LO +3N$_{\rm lnl}$ interaction. The results obtained for the different interactions and methods agree with each other to within about 5%, which is reasonable considering the level of approximation (see methods section discussion of the VS-IMSRG above).

The benchmark for the Gamow-Teller decay of $^{10}$C between NCSM and VS-IMSRG is shown in Tab. IV. Both

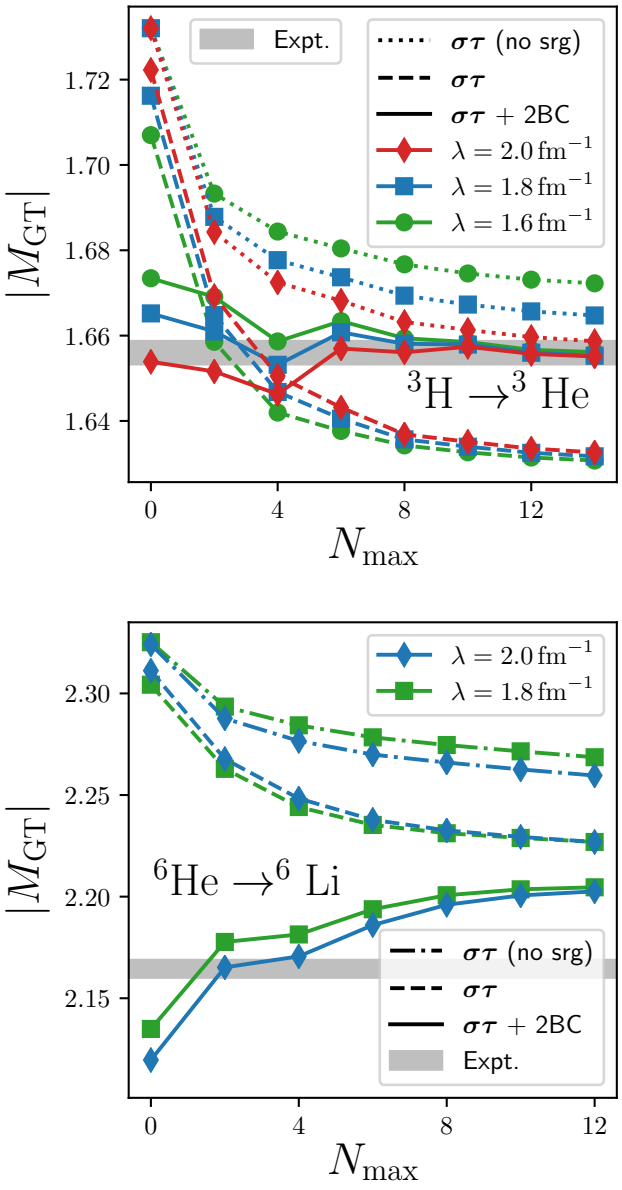


FIG. 8. Convergence of the $^3$H→$^3$He (top panel) and $^6$He→$^6$Li (bottom panel) Gamow-Teller matrix elements with respect to the NCSM basis size for three values of the SRG evolution parameter $\lambda$. Dashed and full lines show results obtained with one-body only and one- plus two-body operators, respectively. The NN-N$^4$LO+3N$_{\mathrm{lnl}}$ interaction was used with both the interaction and transition operators consistently SRG evolved. The dotted lines show results ontained with the same SRG evolved interaction using only the one-body operator without any SRG evolution. The shadow bands represent the experimental values with their uncertainties.

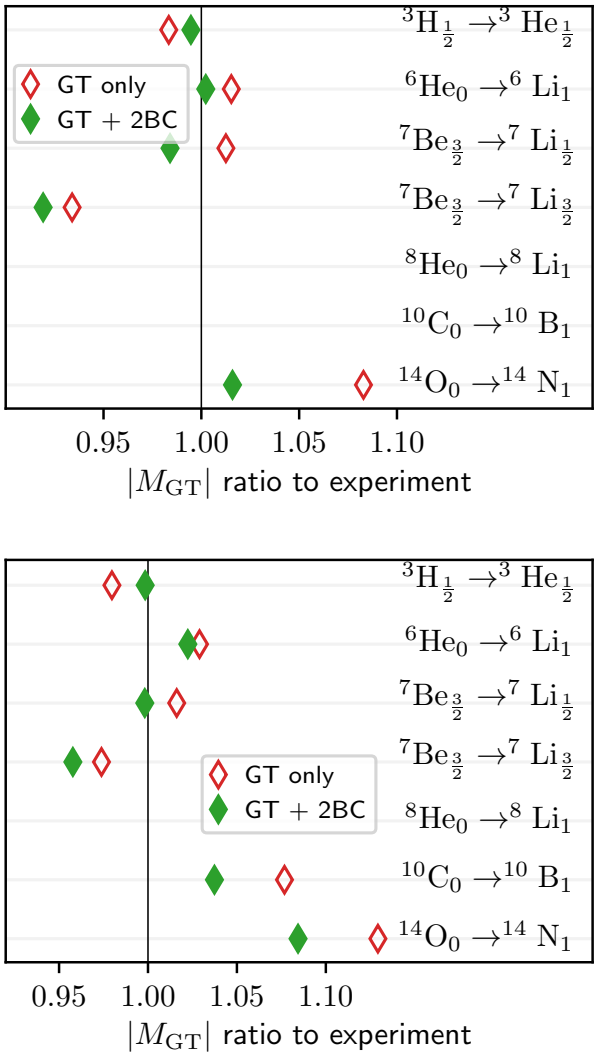


FIG. 9. Theory-to-experiment ratio for the Gamow-Teller matrix elements of six strong transitions in light nuclei for the NNLO$_{\mathrm{sat}}$ (top) and NN-N$^3$LO+3N$_{\mathrm{lnl}}$ (bottom) interactions. The subscripts in the legend denote the total angular momenta of the parent and daughter states. All initial states are ground states. In the case of $^3$H→$^3$He, $^6$He→$^6$Li and $^7$Be→$^7$Li$_{\frac{3}{2}}$, the daughter nucleus is in its ground state, while the $^7$Be→$^7$Li$_{\frac{1}{2}}$ and $^{10}$C→$^{10}$B$_1$ are decays to the first excited state of the daughter nucleus, and the $^{14}$O→$^{14}$N$_1$ is a decay to the second excited state of $^{14}$N. Hollow symbols correspond to results obtained with the standard Gamow-Teller $\sigma\tau$ operator, and full symbols include 2BC. For NNLO$_{\mathrm{sat}}$ (top panel) the value for the $^{10}$C→$^{10}$B$_1$ Gamow-Teller transition are off-scale and not shown.

methods agree with each other within 3%.

For medium-mass nuclei, the comparison between coupled-cluster methods and VS-IMSRG is shown in Tab. V. The CCSDT-1 and VS-IMSRG(2) results are within a few percent for the Gamow-Teller decay of $^{64}$Ni, and within about 20% and 25% for the Gamow-Teller decays of $^{34}$Si to the second and first excited $1^+$ states in $^{34}$P. We note that for the transitions in $^{34}$Si there might be some mixing between the low-lying $1^+$ states

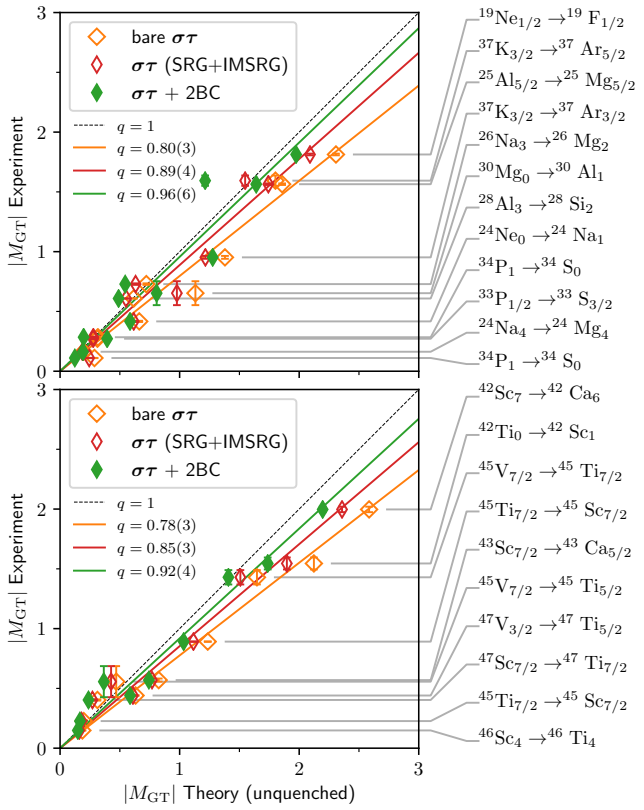


FIG. 10. Comparison of experimental and theoretical Gamow-Teller matrix elements for medium-mass nuclei in the *sd*-shell (top panel) and lower *pf*-shell (bottom panel) for the NN-N$^4$LO+3N$_{\rm lnl}$ interaction. The theoretical results were obtained using (i) a bare Gamow-Teller operator $\boldsymbol{\sigma\tau}$ (no SRG evolution), (ii) a $\boldsymbol{\sigma\tau}$ operator consistently evolved with the Hamiltonian by SRG and IMSRG, and (iii) a consistently-evolved Gamow-Teller operator including 2BC. All expecation values are taken between the same VS-IMSRG wave functions. The linear fits show the resulting quenching factor $q$ given in the panels.

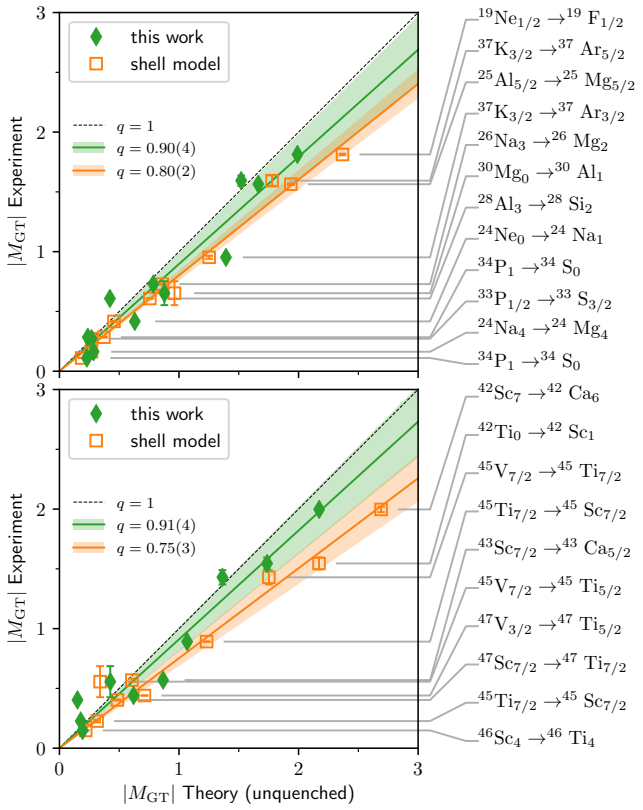


FIG. 11. Same as Fig. 3, except that we employ the NNLO$_{\rm sat}$ interaction in the VS-IMSRG calculations.

in $^{34}$P that is differently accounted for in the CCSDT-1 and VS-IMSRG(2) approaches. To mitigate this effect we consider the square root of the sum of the squared Gamow-Teller strengths to the first two $1^+$ states in $^{34}$P (see e.g. [16, 18]), and obtain $[\sum M^2_{\rm GT}(\boldsymbol{\sigma\tau})]^{1/2} = 1.28$ and 1.18, and $[\sum M^2_{\rm GT}]^{1/2} = 1.0$ and 0.89 for CCSDT-1 and VS-IMSRG(2), respectively.

### Convergence of excited states and Gamow-Teller transitions

Gamow-Teller decays often involve excited states of the daughter nucleus. For this reason we present deatils regarding the quality of our calculations of excited states. Figure 12 shows the convergence of the Gamow-Teller transition of $^{100}$Sn with respect to the active space truncation $\tilde{E}_{pqr} = \tilde{e}_p + \tilde{e}_q + \tilde{e}_r < \tilde{E}_{3\rm max}$ in the three-particle-three-hole excitations in EOM-CCSDT-1 for $N_{\rm max} = 8$ for the 1.8/2.0 (EM) interaction. By comparing with the converged $N_{\rm max} = 10, \tilde{E}_{3\rm max} = 11$ result we see that the Gamow-Teller transitions is converged with respect to both the model-space truncation $N_{\rm max}$ and the active space truncation $\tilde{E}_{pqr}$. This new truncation allows for accelerated convergence with minimal configurations both in ground- and excited-state calculations. Even for the hardest interaction, NNLO$_{\rm sat}$, we find that the result is converged at the 1% level for Gamow-Teller transitions for truncation $N_{\rm max} = 10, \tilde{E}_{3\rm max} = 11$.

TABLE II. Gamow Teller (GT) transition strength in $^8$He to the first $1^+_1$ in $^8$Li for the NN-N$^4$LO +3N$_{\rm lnl}$ interaction calculated in the EOM-CCSDT-1, VS-IMSRG(2), and NCSM approaches.

| Method | $\lvert M_{\rm GT}(\boldsymbol{\sigma\tau})\rvert$ | $\lvert M_{\rm GT}\rvert$ |
|---|---|---|
| EOM-CCSD | 0.45 | 0.48 |
| EOM-CCSDT-1 | 0.42 | 0.45 |
| VS-IMSRG(2) | 0.54 | 0.58 |
| NCSM | 0.41 | 0.46 |

Figure 13 shows the convergence of the $^7$Be$\to^7$Li$_{\frac{3}{2}}$ and

TABLE III. Gamow Teller (GT) transition strength in $^{14}$O to the second $1_2^+$ in $^{14}$N for the NNLO$_{\rm sat}$ and NN-N$^4$LO +3N$_{\rm lnl}$ interactions calculated in the EOM-CCSDT-1, VS-IMSRG, and NCSM approaches.

| Interaction | NNLO$_{\rm sat}$ | | NN-N$^4$LO+3N$_{\rm lnl}$ | |
|---|---|---|---|---|
| Method | $\lvert M_{\rm GT}(\boldsymbol{\sigma\tau})\rvert$ | $\lvert M_{\rm GT}\rvert$ | $\lvert M_{\rm GT}(\boldsymbol{\sigma\tau})\rvert$ | $\lvert M_{\rm GT}\rvert$ |
| EOM-CCSD | 2.15 | 2.08 | 2.26 | 2.06 |
| EOM-CCSDT-1 | 1.77 | 1.69 | 1.97 | 1.86 |
| VS-IMSRG(2) | 1.72 | 1.76 | 1.83 | 1.83 |
| NCSM | 1.80 | 1.69 | 1.86 | 1.78 |

TABLE IV. Gamow Teller (GT) transition strength in $^{10}$C to the first $1_1^+$ in $^{10}$B for the NN-N$^4$LO +3N$_{\rm lnl}$ interaction calculated in the VS-IMSRG(2) and NCSM approaches.

| Method | $\lvert M_{\rm GT}(\boldsymbol{\sigma\tau})\rvert$ | $\lvert M_{\rm GT}\rvert$ |
|---|---|---|
| VS-IMSRG(2) | 1.94 | 1.88 |
| NCSM | 2.01 | 1.92 |

$^7$Be$\rightarrow^7$Li$_{\frac{1}{2}}$ Gamow-Teller matrix elements with respect to the NCSM basis size. By looking at the convergence trend with increasing model-space size it is conceivable that the effect of 2BC could slightly enhance (instead of quench) the Gamow-Teller matrix element for the $^7$Be$\rightarrow^7$Li$_{\frac{3}{2}}$ transition, bringing this result closer to those of Ref. [26]. Finally Fig. 14 shows the convergence of the Gamow-Teller matrix element for the transition $^{24}$Al$\rightarrow^{24}$Mg with increasing model-space size calculated with the VS-IMSRG approach.

Figure 15 shows the convergence of excited states in the daughter nucleus $^{100}$In using the EOM-CCSDt-1 and the EOM-CCSDT-1 approaches with $\tilde{E}_{\rm 3max}$. We clearly see a dramatic acceleration in convergence with the EOM-CCSDt-1 approach compared to the EOM-CCSDT-1 approach with respect to $\tilde{E}_{\rm 3max}$.

### Fermi gas model

The Fermi-gas model is one of the simplest approaches to atomic nuclei. To throw further light onto the quenching factors we obtained from 2BC, we compare the results of our sophisticated many-body calculations with estimates from this simple model. In the Fermi-gas model of Ref. [71] the quenching due to 2BC is

$$q_{\rm 2BC} \approx 1 - \frac{\rho}{F_\pi^2}\left[-\frac{c_D}{4g_A\Lambda_\chi} + \frac{I(\rho)}{3}\left(2c_4 - c_3 + \frac{1}{2m}\right)\right], \tag{15}$$

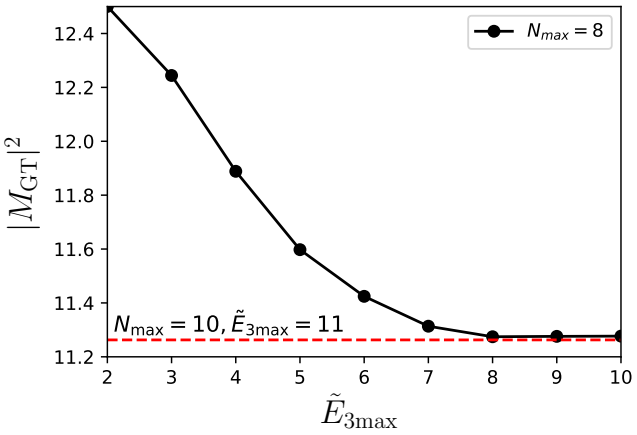


FIG. 12. Convergence of the EOM-CCSDT-1 calculation of the Gamow-Teller transition of $^{100}$Sn with respect to the active space truncation $\tilde{E}_{\rm 3max}$ of the three-particle-three-hole excitations in the EOM-CCSDT-1 approximation for $N_{\rm max} = 8$ for the 1.8/2.0 (EM) interaction. The horizontal line shows the converged $N_{\rm max} = 10, \tilde{E}_{\rm 3max} = 11$ result.

with

$$I(\rho) = 1 - \frac{3m_\pi^2}{k_F^2} + \frac{3m_\pi^3}{k_F^3}\arctan(k_F/m_\pi) \tag{16}$$

and

$$\rho = \frac{2k_F^3}{3\pi^2}. \tag{17}$$

Here, we employed the relationship between 2BC and 3N forces with the correct factor $-1/4$ for the short range term proportional to $c_D$ as given in Ref. [72]. In Eqs. (15) to (17), $\rho$ is the density, $k_F$ the Fermi momentum, and $I(\rho)$ is a function of $\rho$. We have $\rho = 0.16$ fm$^{-3}$, $k_F = 1.33$ fm$^{-1}$, and $I(\rho) \approx 0.65$ at nuclear matter saturation, $F_\pi = 92.4$ MeV the pion-decay constant, $m = 939$ MeV the nucleon mass, $g_A = 1.27$, and $\Lambda_\chi = 700$ MeV. The pion-nucleon couplings $c_3$ and $c_4$ yield a value $2c_4 - c_3$ of about 11 to 15 GeV$^{-1}$ for a wide range of EFT interactions (see Table VI and Methods for details). These contributions have been considered early on (see, e.g., Ref. [4]), and in our EFT-based calculations give the dominant contributions from 2BC to the quenching. The 2BC contribution proportional to $c_D$ is set by shorter-range 3N forces and is found to be small, which counters the quenching from the long-range part of the 2BC. We note that acceptable nuclear saturation favors values for $c_D$ that are positive and of order one, and we have $0.7 \lesssim c_D \lesssim 1.3$ for the EFT interactions we employ (except for the NN-N$^4$LO+3N$_{\rm lnl}$ and 2.0/2.0 (PWA), see Table VI below and Methods).

We can attempt to relate the results displayed in Fig. 1 and Table I to the Fermi gas model. For this purpose we show in Table VI the relevant low-energy couplings that

TABLE V. Gamow Teller (GT) transition strengths in $^{34}$Si and $^{68}$Ni for the NN-N$^4$LO +3N$_{\rm lnl}$ interaction calculated in the EOM-CCSDT-1 and VS-IMSRG approaches.

| | $^{34}$Si→$^{34}$P$_{1_1^+}$ | | $^{34}$Si→$^{34}$P$_{1_2^+}$ | | $^{68}$Ni→$^{68}$Cu$_{1_1^+}$ | |
|---|---|---|---|---|---|---|
| Method | $\lvert M_{\rm GT}(\boldsymbol{\sigma\tau})\rvert$ | $\lvert M_{\rm GT}\rvert$ | $\lvert M_{\rm GT}(\boldsymbol{\sigma\tau})\rvert$ | $\lvert M_{\rm GT}\rvert$ | $\lvert M_{\rm GT}(\boldsymbol{\sigma\tau})\rvert$ | $\lvert M_{\rm GT}\rvert$ |
| EOM-CCSD | 0.61 | 0.28 | 1.32 | 1.14 | 0.60 | 0.46 |
| EOM-CCSDT-1 | 0.56 | 0.28 | 1.15 | 0.96 | 0.42 | 0.35 |
| VS-IMSRG(2) | 0.78 | 0.52 | 1.00 | 0.85 | 0.42 | 0.36 |

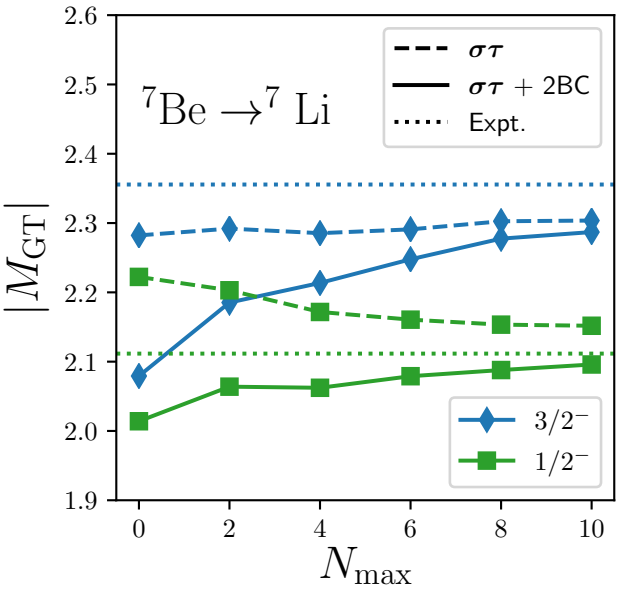


FIG. 13. Convergence of the $^7$Be$\rightarrow^7$Li$_{\frac{3}{2}}$ and $^7$Be$\rightarrow^7$Li$_{\frac{1}{2}}$ Gamow-Teller matrix elements with respect to the NCSM basis size. Dashed and full lines show results obtained with one-body only and one- plus two-body operators, respectively. The dotted lines represent the experimental values. The NN-N$^4$LO+3N$_{\rm lnl}$ interaction was used with both the interaction and transition operators consistently SRG evolved.

enter Eq. (15), both for the EFT interactions used in this work and for other interactions that yielded little contributions from 2BC. We note that the contributions from the pion-exchange 2BC (proportional to $2c_4 - c_3$) vary less than those from the short-ranged 2BC (proportional to $c_D$).

Figure 16 shows the quenching factor based on Eq. (15) for interactions as indicated (compare to Table VI for references). The full red symbols are for a density $\rho = 0.08$ fm$^{-3}$ (typical for the nuclear surface), and the full red line shows a linear fit to the points. The hollow blue symbols and dashed line show the corresponding results at the saturation density $\rho = 0.16$ fm$^{-3}$. The contributions of 2BC are proportional to the density $\rho$.

In Fig. 17 we show the Gamow-Teller transition strength in $^{100}$Sn as a function of the low-energy coupling $c_D$ for the interaction 1.8/2.0 (EM) computed in the charge-exchange EOM-CCSDT-1 approach. For $c_D = 0$ the extracted quenching factor is $q_{\rm 2BC} = 0.77$, and for the full 2BC ($c_D = 1.264$) it is $q_{\rm 2BC} = 0.79$. This demonstrates that the majority of the quenching from 2BC comes from the long-range pion-exchange 2BC, while the short-range part gives a smaller contribution.

This accounting is further analyzed in Fig. 18. Here, the quenching factor for the Gamow-Teller transition in $^{100}$Sn is shown as a function of $c_D$ for the Fermi-gas model at a density $\rho = 0.08$ fm$^{-3}$ and EOM-CCSDT-1 using the same interaction. We observe that the simple interpretation of quenching in terms of the Fermi-gas model is validated in this nucleus because both approaches yield the same linear trend and similar values for the quenching as a function of the low-energy coupling $c_D$.

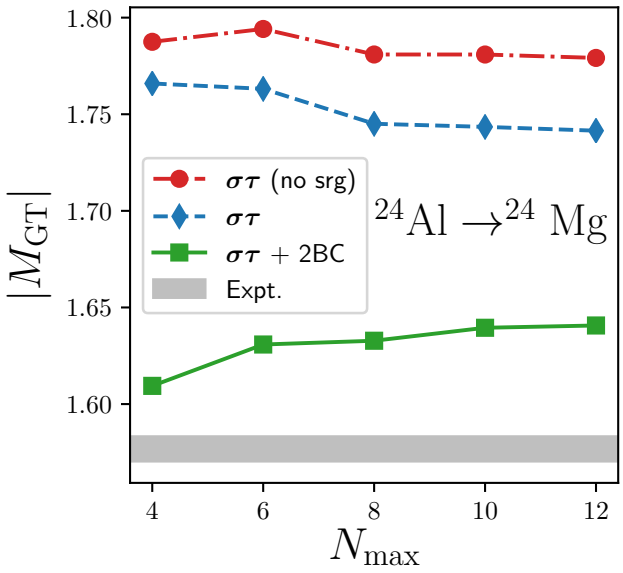


FIG. 14. Convergence of the Gamow-Teller matrix element for $^{24}$Al$\rightarrow^{24}$Mg calculated with the VS-IMSRG, as a function of the number of harmonic oscillator shells used.

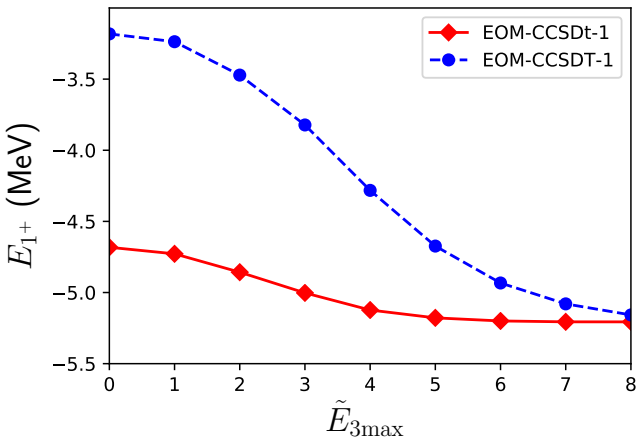


FIG. 15. Convergence of the first excited $1^+$ state in $^{100}$In with respect to the ground-state energy of $^{100}$Sn for increasing $\tilde{E}_{3\rm max}$ using the EOM-CCSDT-1 (blue dashed line) and EOM-CCSDt-1 (red solid line) approaches. Here the single-particle model-space was given by $N_{\rm max} = 8$, and we employed the 1.8/2.0 (EM) interaction.

TABLE VI. Values of the low-energy coupling $c_D$, the combination $2c_4 - c_3$ of pion-nucleon couplings, and the value of $\Lambda_\chi$ that enters the simple estimate (15) of the renormalization of the axial-vector coupling due to 2BC. The first seven EFT interactions are used in this work, and the latter are other interactions (for details see the references given).

| Interaction | $c_D$ | $2c_4 - c_3$ | $\Lambda_\chi$ [GeV] | Ref. |
|---|---|---|---|---|
| $\mathrm{NNLO_{sat}}$ | 0.817 | 11.46 | 0.7 | [24] |
| NN-N$^4$LO +3N$_{\mathrm{lnl}}$ | −1.8 | 13.88 | 0.7 | |
| NN-N$^3$LO +3N$_{\mathrm{lnl}}$ | 0.7 | 14.0 | 0.7 | [25] |
| 1.8/2.0 (EM) | 1.264 | 14.0 | 0.7 | [23] |
| 2.0/2.0 (EM) | 1.271 | 14.0 | 0.7 | [23] |
| 2.2/2.0 (EM) | 1.214 | 14.0 | 0.7 | [23] |
| 2.0/2.0 (PWA) | −3.007 | 12.7 | 0.7 | [23] |
| Pastore 500 | −1.847 | 14.0 | 1.0 | [26] |
| Pastore 600 | −2.03 | 14.13 | 1.0 | [26] |
| Ekström 450 | 0.0004 | 13.22 | 0.7 | [50] |
| Ekström 500 | 0.0431 | 12.50 | 0.7 | [50] |
| Ekström 550 | 0.1488 | 11.71 | 0.7 | [50] |

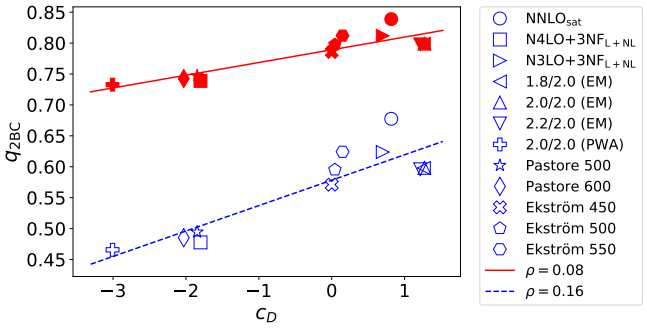


FIG. 16. Quenching factor $q_{\mathrm{2BC}}$ obtained from Eq. (15) for the EFT interactions considered in this work as well as from Refs. [50], [26] (see Table VI), at two different densities $\rho = 0.08$ fm$^{-3}$ and $\rho = 0.16$ fm$^{-3}$.

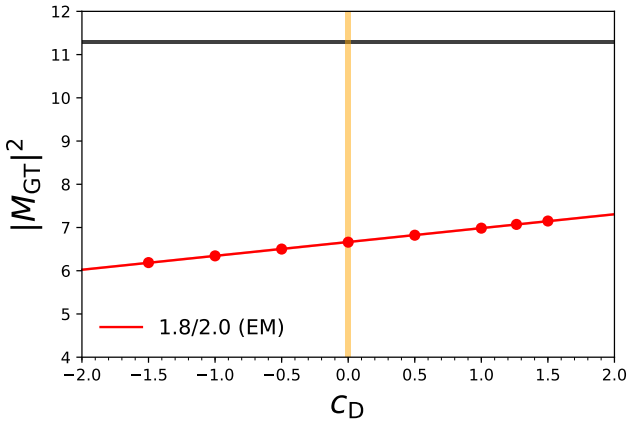


FIG. 17. Gamow-Teller strength $|M_{\rm GT}|^2$ in $^{100}$Sn as a function of the low-energy coupling $c_D$ for the 1.8/2.0 (EM) interaction. The horizontal black line gives the result for the Gamow-Teller strength for the standard Gamow-Teller operator ($\boldsymbol{\sigma\tau}$) only. As can been seen, the quenching from the pion-exchange 2BC alone ($c_D = 0$) is $q_{\rm 2BC} = 0.77$, and for the full 2BC ($c_D = 1.264$) it is $q_{\rm 2BC} = 0.79$. Thus the majority of the quenching from 2BC comes from the long-range pion-exchange part.

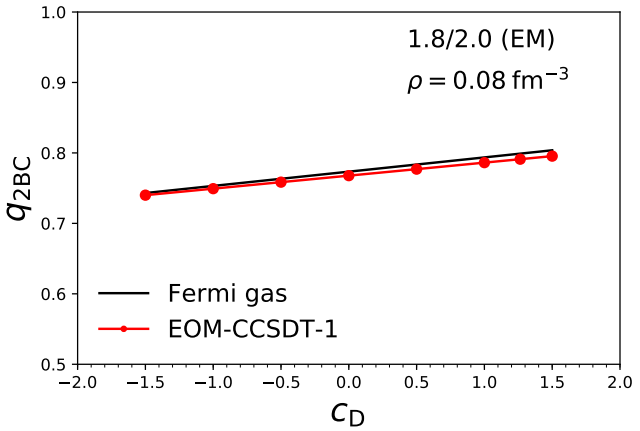


FIG. 18. Quenching factor $q_{\rm 2BC}$ as a function of the low-energy coupling $c_D$ for the 1.8/2.0 (EM) interaction. The black line gives the quenching factor obtained with the Fermi-gas model and the red line gives the quenching factor obtained in the EOM-CCSDT-1 method.